ENGINEERING

Local lateral contact governs shear traction of micropatterned surfaces on hydrogel substrates

Kristin N. Calahan[1,2]†, Yuan Qi[1]†, Karl G. Johannes[1], Mark E. Rentschler[1]*, Rong Long[1]*

Micropatterned surfaces exhibit enhanced shear traction on soft, aqueous tissue-like materials and, thus, have the potential to advance medical technology by improving the anchoring performance of medical devices on tissue. However, the fundamental mechanism underlying the enhanced shear traction is still elusive, as previous studies focused on interactions between micropatterned surfaces and rigid substrates rather than soft substrates. Here, we present a particle tracking method to experimentally measure microscale three-dimensional (3D) deformation of a soft hydrogel in normal and shear contact with arrays of microscale pillars. The measured 3D strain and stress fields reveal that the lateral contact between each individual pillar and the deformed hydrogel substrate governs the shear response. Moreover, by comparing pillars with different cross-sectional geometries, we observe experimental evidence that the shear traction of a pillar on the hydrogel substrate is sensitive to the convex features of its leading edge in the shear direction.

INTRODUCTION

Friction plays a fundamental role in biological systems at tissue-tissue interfaces (e.g., cartilage) (*1*, *2*) and in biomedical applications at tissue-device interfaces (*3*). Numerous medical devices interface directly with tissue and rely on a specified, or repeatable, anchoring force for proper function. For example, devices such as stents and balloon catheters need to be anchored at tissue surfaces to prevent slippage (*4*). Recent engineering developments have enabled medical robots with in vivo mobility that require adequate shear traction on tissue for locomotion (*5*). Micropatterned surfaces (*6*–*8*) have been implemented on devices, such as medical robots (*9*, *10*), for enhanced traction performance in lubricated and deformable tissue environments. While micropatterned surfaces with periodic pillar arrays or random biomimetic features have been widely studied, most of the literature has focused on their contact against a rigid substrate (e.g., glass) (*11*–*14*). The limited studies that consider a compliant substrate, such as biological tissue or silicone elastomers, show that pillar geometry (e.g., size and shape) often influences contact at the interface and, thus, affects the traction performance (*15*–*17*).

The frictional contact with soft materials is highly relevant for biological systems (*18*–*20*) and is vastly different from that with rigid substrates due to large deformation, material nonlinearity, and time-dependent properties of the soft materials. Experimental studies, using hydrogels as a tissue model, have determined that there are many parameters that contribute to hydrogel friction including loading parameters (*21*–*23*), surface conditions (*24*–*26*), and material properties (*27*–*29*). In particular, sliding velocity is a key loading parameter that has been extensively studied because it determines the type of interface lubrication and the contributions of bulk viscoelasticity or poroelasticity. On the contrary, for medical stents or balloon catheters, the anchoring performance under static contact or low-velocity sliding is more relevant, where the geometry and mechanics of contact play the dominating role. Unlike spherical indentation often adopted in existing studies, the contact between a micropatterned surface (e.g., an array of flat-ended pillars) and a soft substrate involves complex asymmetrical three-dimensional (3D) deformation. For example, it has been hypothesized that a buildup of substrate material at the leading edge of a pillar may occur upon normal and shear loading, which forms a barricading structure contributing to the total traction (*17*). However, experimental data directly capturing such intricate 3D deformation fields are lacking.

Mapping 3D deformation fields in soft gels is a challenging task but has been demonstrated by combining confocal microscopy with various techniques including hyperelastic warping (*30*), finite element–based methods (*31*), digital volume correlation (*32*–*35*), and traction force microscopy (*36*–*39*). While several of these methods have proven successful for 3D small deformation with limited geometrical nonlinearity, full-field measurement of 3D large deformation remains a challenge. Here, we present an experimental method to reveal how 3D large deformation in a hydrogel substrate upon contact with micropatterned surfaces leads to enhanced shear traction for anchoring. Specifically, we use confocal microscopy and a custom-built microindentation and visualization (MIV) system (fig. S1) (*40*) to track fluorescent particles embedded in a polyacrylamide hydrogel substrate upon contact with flat-ended pillars fabricated using polydimethylsiloxane (PDMS) elastomer. After tracking the particles, we implement an interpolation scheme to generate continuous 3D displacement fields from discrete particle displacements, obtain the 3D strain fields by taking spatial derivatives of the interpolated displacement fields, and determine the 3D stress fields and surface traction maps by applying a constitutive model. The surface traction maps allow us to study the interaction of individual pillars with the hydrogel substrate and identify geometric attributes that are important for the enhanced shear traction.

RESULTS

Shear traction of micropatterned surfaces on hydrogel

The PDMS pillars [Young's modulus = 3 MPa (*41*)] studied here are 100 μm in height with flat-end surfaces and sharp edges (fig. S2). Various geometries are considered as illustrated by representative scanning electron microscopy (SEM) images in Fig. 1A. The circle,

[1]Department of Mechanical Engineering, University of Colorado Boulder, Boulder, CO 80309, USA. [2]BioFrontiers Institute, University of Colorado Boulder, Boulder, CO 80309, USA.
*Corresponding author. Email: mark.rentschler@colorado.edu (M.E.R.); rong.long@colorado.edu (R.L.)
†These authors contributed equally to this work.

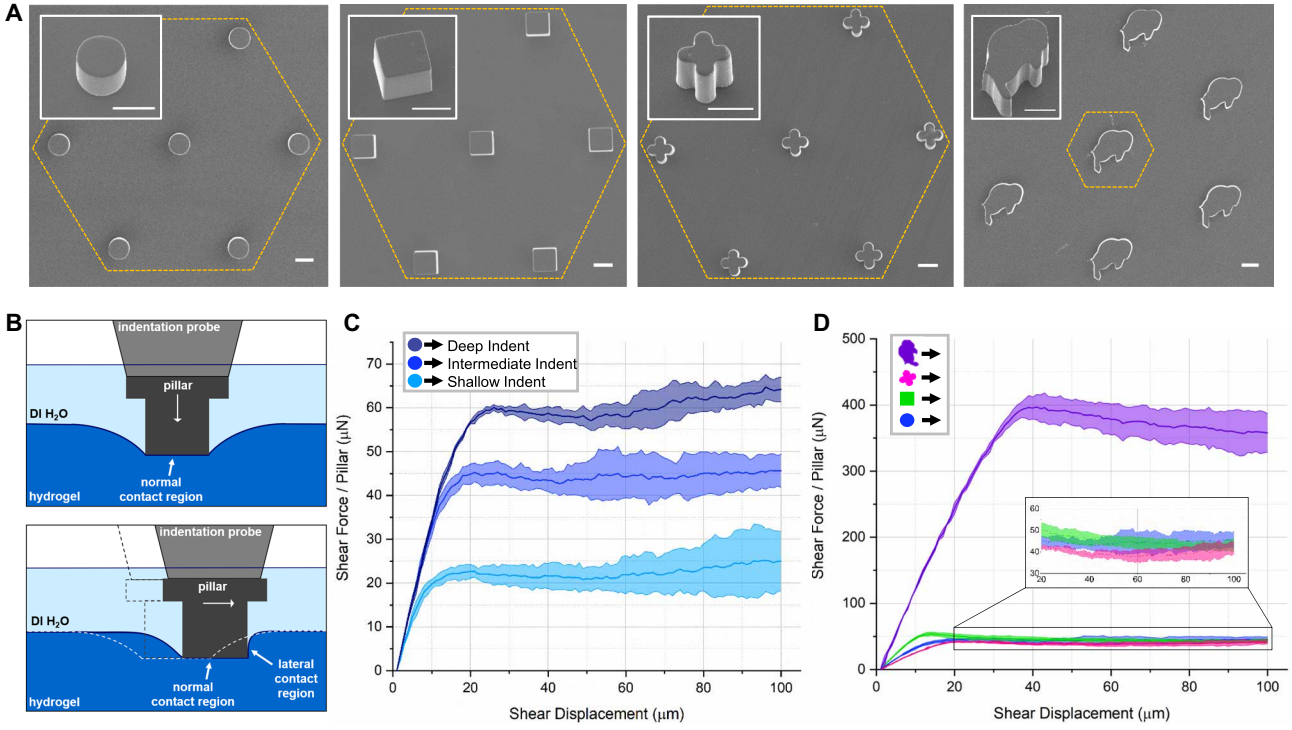

Fig. 1. Indentation and shear experiments suggest lateral contact mechanism. (**A**) Scanning electron microscope images of PDMS pillar surfaces highlighting individual pillar cross-sectional geometries (from left to right: circle, square, clover, and buffalo). The dashed orange hexagon shape outlines the pillar probes used for each geometry in all experiments. Scale bars, 100 μm. (**B**) Hypothesized lateral contact mechanism (bottom) of a pillar on a hydrogel substrate following normal indentation (top). The shear displacement causes the pillar's lateral surface to engage the deformed hydrogel surface and, hence, establishes lateral contact. A single pillar on the indentation probe is shown in this schematic for clarity. (**C**) Shear force per pillar versus shear displacement from the benchtop experiments (continuous loading) with circular pillars at varying normal indentation depths. (**D**) Shear force per pillar versus shear displacement from the benchtop experiments (continuous loading), with different pillar geometries at the intermediate indentation depth. The black arrows in the legends of (C) and (D) denote the direction of shear displacement relative to the pillar cross section. The solid lines and shaded areas in (C) and (D) represent the means and SDs of shear force at a given shear displacement obtained from three repeated experiments.

square, and clover geometries were designed with equal cross-sectional widths (140 μm), while the buffalo geometry, included here as an example for asymmetric pillar geometry, required a width about two times that of the other geometries to ensure that the smaller features were fabricated with fidelity. We used the MIV system to measure the PDMS pillars' shear tractions on soft polyacrylamide hydrogel substrates (Young's modulus = 102 kPa) submerged in deionized water. Briefly, probes of the pillar surfaces were first indented into the hydrogel substrate normal to the substrate surface, after which a shear displacement parallel to the substrate surface was applied with the normal indentation depth held fixed. This process was conducted under continuous displacement loading with a fixed velocity (0.2 μm/s) along both the normal and shear directions. For each pillar geometry, we performed tests to obtain the shear forces at shallow (13 to 18 μm), intermediate (33 to 38 μm), and deep (53 to 58 μm) normal indentations before the shear loading. The small variations in the normal indentation depth (within 5 μm) in each group of tests are due to uncertainty of the manual surface finding method. We will refer to this set of experiments as the "benchtop experiments" (see the "Benchtop experiments" section) to distinguish them from the confocal microscopy experiments described later.

As a control, we measured the shear force of a flat PDMS surface on the same hydrogel substrate following the same procedures and found the average shear stress to be over 20 times less than that of the circular pillar surface (section S1 and fig. S3). Despite the smaller actual contact area, the pillar surface still exhibited a profound increase in the average shear stress in comparison to the flat control. This result implies that the shear force for pillar surfaces does not rely on the intrinsic friction of the hydrogel substrate. Rather, we hypothesize that, upon shear loading, the lateral surface of a pillar can engage the deformed hydrogel surface, forming a lateral contact region at the leading edge of the pillar (Fig. 1B), which is reminiscent of the ploughing effect in metallic friction (*42*, *43*). The normal contact pressure within the lateral contact region provides the primary contribution to the total shear force of each pillar. Motivated by this hypothesis, we divided the measured shear force (fig. S4) by the respective number of pillars on each probe. The probes for circular, square, and clover pillar all consisted of seven pillars arranged in a hexagonal pattern, while the probe for buffalo pillar consisted of one pillar because of its larger size (Fig. 1A and table S1). The resulting shear force per pillar (fig. S5) was used to examine the effects of indentation depth and pillar geometry. First, the shear force per pillar for circular pillars increased as the pillars were indented further into the hydrogel substrate (Fig. 1C). Second, the shear force per pillar for different pillar geometries collected at the intermediate indentation depth (33 to 38 μm) is plotted in Fig. 1D, highlighting the important role of pillar geometry in determining the shear force per pillar. In particular, the purple curve, representing the

buffalo pillar with the posterior side as the leading edge, substantially exceeds those for the other pillar geometries.

Results of the benchtop experiments show that the single-pillar level contact mechanics with the hydrogel substrate is important for shear traction enhancement. On the basis of the lateral contact hypothesis, we anticipate that indentation depth can affect the size of lateral contact by controlling the extent of substrate deformation. The effect of pillar geometry, however, is more nuanced. For example, we scaled the shear force per pillar (section S2) by the cross-sectional area of each pillar geometry and found that the scaled shear force differed substantially between pillar geometries (fig. S6) despite the similar level of average normal contact pressure (fig. S7), which further confirms that the shear force did not come from friction at the bottom surface of the pillar. According to the lateral contact hypothesis, the width of the pillars' leading edge toward the shear direction should be more relevant for determining the shear force per pillar. Therefore, we scaled the shear force per pillar by the projected width of the pillars' leading edge (fig. S8) but still observed large differences between pillar geometries, implying that the detailed geometry of leading edge is also important. In particular, the four pillar geometries included in Fig. 1D exhibit leading edge shapes that vary from convex (circle or clover) to flat (square) to jagged (buffalo). The "jagged" shape refers to the posterior side of the buffalo geometry featuring multiple protrusions (e.g., the legs). It appears that the buffalo pillar with jagged leading edge gave the largest shear force per pillar. Although results of the benchtop experiments are all consistent with the lateral contact hypothesis, direct experimental evidence is still lacking. In addition, a physical picture on how the pillar geometry affects the lateral contact remains elusive. To address these limitations, we use a particle tracking method, as demonstrated in the next section, to measure the 3D deformation fields within the hydrogel substrate upon contact with the pillars.

Measuring 3D deformation fields with particle tracking and deducing stress fields

The particle tracking method is demonstrated and validated using a benchmark problem: normal indentation of a rigid sphere on the hydrogel substrate (Fig. 2A). The spherical indenter was a steel ball (500 μm in diameter) coated with a thin layer of fluorescently dyed PDMS and glued to an aluminum indentation probe (Fig. 2B). The indenter was displaced along the Z direction at a velocity of 0.2 μm/s, slow enough to minimize dynamic effects, into the hydrogel substrate (*40*). During this experiment, the MIV system was integrated on the stage of a laser scanning confocal microscope (LSCM), which enables 3D image acquisition of the contact interface (see the "Confocal microscopy experiments" section). These experiments used a stepwise loading scheme because it took ~30 min to acquire a single 3D image stack at the resolution required for particle tracking. A total displacement of 100 μm in the negative Z direction was applied at increments of 10 μm. A 3D image stack was acquired at each step, capturing the fluorescent tracer particles embedded in the hydrogel substrate (Fig. 2C). During postprocessing of the acquired image stacks, the 3D distributions of fluorescence intensity were used to locate the centroids of tracer particles, which were then tracked over time using IMARIS (Bitplane, Zürich, Switzerland). In addition, the MIV system recorded the normal (Z) and shear (X) forces from the two-axis load cell and the normal (Z) and shear (X) displacements from each piezoelectric actuator (Fig. 2D). For this experiment, zero shear displacement along the X direction was applied to the spherical indenter. The measured force data show a step-like relaxation behavior reflecting the stepwise displacement loading. Specifically, the image acquisition time (~30 min) was sufficient for the hydrogel to relax under the fixed displacement, causing the decrease in force.

The centroids of fluorescent tracer particles were tracked through the image series using the spots tool and autoregressive motion algorithm in IMARIS (see the "Image processing" section). Individual tracks for each particle reveal particle displacements, resulting in a set of discrete displacement data at each loading step (Fig. 2E). The number of tracked particles influences the spatial resolution of the resulting 3D deformation fields. For this experiment, there were nearly 6000 tracer particles tracked through the image series.

Continuous displacement fields were constructed from discrete displacement data (extracted from tracer particle displacements in the postprocessed image stacks) at each time step using the moving least square (MLS) scheme (*44*). The 3D strain fields were calculated by taking spatial gradients of the continuous 3D displacement field after interpolation (*45*–*47*). During indentation, the hydrogel substrate may undergo large deformation. We account for geometric nonlinearity using the theory of finite strain kinematics to calculate the Hencky strain (or true strain) tensor $\boldsymbol{\varepsilon}$ (see the "Particle tracking method" section). To derive 3D stress fields from the experimentally measured 3D strain fields, we treat the hydrogel substrate as a compressible neo-Hookean solid to establish the stress-strain relation, because the long imaging time renders the hydrogel at its long-term relaxed limit by allowing sufficient time for solvent migration (i.e., poroelastic relaxation). This constitutive relation contains only two parameters: shear modulus μ and Poisson's ratio ν at small strain, both of which were experimentally calibrated (μ = 37.5 kPa and ν = 0.362; see section S3). Equipped with the calibrated stress-strain relation, we were able to determine the Cauchy stress (or true stress) fields $\boldsymbol{\sigma}$ in the hydrogel substrate from the measured strain fields.

We examined the accuracy of the experimentally derived 3D fields by calculating the total reaction forces on the hydrogel substrate from the deduced stress fields. Briefly, we first identified the normal vector $\mathbf{n}$ at a given point on the surface of the deformed hydrogel substrate and evaluated the traction vector $\mathbf{t}$ at this point using $\mathbf{t} = \boldsymbol{\sigma}\mathbf{n}$, where $\boldsymbol{\sigma}$ is the deduced Cauchy stress tensor. Integrating $\mathbf{t}$ over the substrate surface results in the total reaction force $\mathbf{F}$. The dominant component of the reconstructed forces (F_z) shows good agreement with the measured values recorded from the two-axis load cell (Fig. 2D). Despite the fact that F_y was not directly measured by the two-axis load cell, the 3D stress fields allow us to determine F_y, which is on the same order of F_x and much smaller than F_z as expected. We expect F_x and F_y to remain zero due to the symmetry of the spherical indentation, as confirmed by the F_x data measured by the load cell (Fig. 2D). However, the reconstructed F_x and F_y deviated from zero at certain loading steps, which is attributed to the large noise-to-signal ratio. In comparison to the dominant component F_z, the reconstructed F_x and F_y showed similar levels of noise but had much smaller magnitudes. This phenomenon can be traced back to the smaller magnitudes of u_x (or u_y) than u_z, because u_z is the dominant displacement component under normal indentation. Furthermore, we compared the experimentally mapped 3D fields of the dominant components of displacement, strain, and stress (i.e., u_z, ε_{zz}, and σ_{zz}) (top row of Fig. 2F), with the corresponding results of a finite element model (bottom row of Fig. 2F) established in Abaqus (v2017; Simulia, Providence, RI), as described in the "Finite element model" section (fig. S11). Despite the scatters in the experimentally

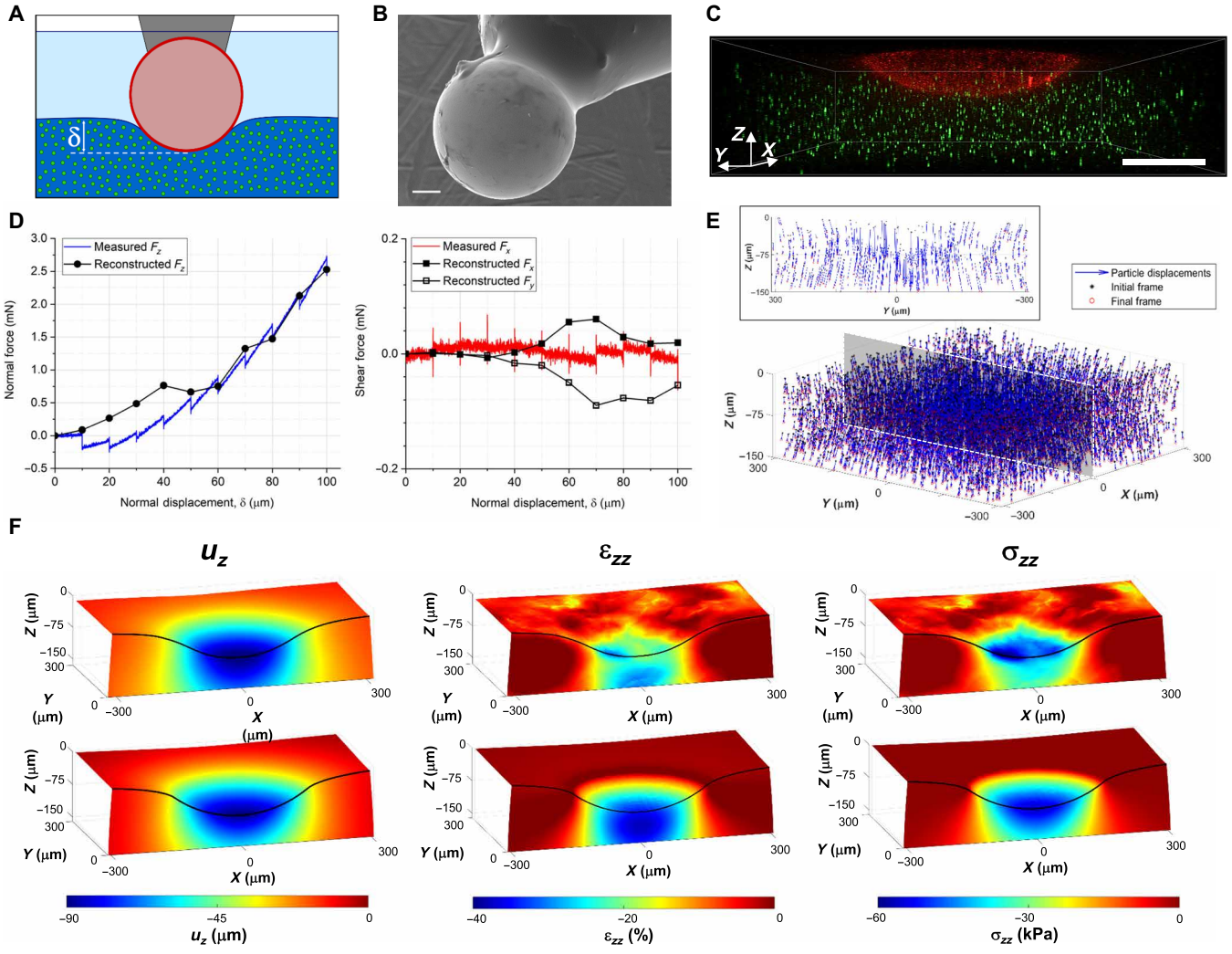

Fig. 2. Validation of the particle tracking method with a spherical indenter. (**A**) Schematic of normal indentation with a PDMS-coated spherical indenter on a hydrogel substrate. (**B**) Scanning electron microscope image of the PDMS-coated spherical indenter. Notice the defects on the surface of the sphere from the PDMS-coating process. Scale bar, 100 μm. (**C**) Raw confocal microscopy image stack at 50-μm normal displacement. The PDMS-coated spherical indenter is shown in red fluorescence and the embedded tracer particles in the hydrogel network are shown in green fluorescence. Scale bar, 100 μm. (**D**) Normal (left) and shear (right) force versus normal displacement reconstructed from the 3D stress fields determined by the particle tracking method (symbols). The normal and shear forces independently measured by the two-axis load cell are shown as solid lines for comparison. (**E**) Representative 3D discrete displacement field generated from particle tracking between the initial frame (with zero normal displacement) and the final frame (with 100-μm normal displacement). The cross section along the *YZ* plane is shown in the inset. (**F**) 3D fields of displacement (u_z), strain (ε_{zz}), and stress (σ_{zz}) fields derived from the particle tracking method (top row) compared to finite element simulation results with matched material parameters (bottom row). The same color bar is applied to the experimental and finite element results to facilitate comparison.

derived fields of ε_{zz} and σ_{zz}, the two sets of results closely resemble each other quantitatively.

The benchmark example not only supports the validity of the 3D particle tracking method but also reveals the possibility of scatters in the resulting strain and stress fields (figs. S12 and S13). A potential explanation for the scatters is the heterogeneous micro- or nanostructures in the hydrogel, which can be assessed by SEM imaging (*48*–*50*). For the polyacrylamide gels used in our work, the heterogeneity length scale has been found to be on the order of 10 to 100 nm through SEM imaging (*51*). In addition, experiments based on quantum dot tracking confirmed the ~100-nm heterogeneity length scale in polyacrylamide gels (*52*). This heterogeneity length scale (10 to 100 nm) is several orders of magnitude smaller than the characteristic length scale in our experiment (~100 μm; e.g., contact area size), implying that the gel substrate can be treated as a homogenized continuum. Therefore, we attribute the scatters in the strain and stress fields to experimental error or uncertainty of the particle tracking method, which may come from multiple sources. Apart from obvious ones such as imaging resolution, centroid finding, and false tracking, we emphasize that the density of tracked particles is an important factor that can influence the step of interpolating the discrete displacement data into a continuous field (*45*). We estimate the average distance between tracer particles to be 23 μm based on our data. Although errors in the displacement fields are relatively small (figs. S12 and S13), it can be carried through the interpolation process and amplified in the strain and stress

fields when we take spatial gradients of the interpolated displacement fields.

Lateral contact region governs shear force

After validation by spherical indentation, the same particle tracking method was used to investigate how indentation depth influences the shear force of a single pillar. Using the circular pillar (Fig. 3A), we varied the normal indentation depth before shear loading from shallow (17 μm), intermediate (36 μm), to deep (55 μm) indentation and performed confocal microscopy imaging. The same pillar probe in the benchtop experiments was used for the confocal microscopy experiments, but the imaging window was focused on the central pillar of the hexagonal array to study the contact mechanics of a single pillar. The shear force per pillar data in these imaging experiments (Fig. 3B) show a step-like relaxation pattern due to the stepwise loading scheme used to allow sufficient time for image acquisition (~30 min). Between loading steps, we observed relaxation of the shear force. Because rheological data in the literature suggest that the cross-linked polyacrylamide network should behave elastically (*53*, *54*), we attribute the relaxation to poroelastic flow often observed for polyacrylamide hydrogels (*55*, *56*). Briefly, the pressure gradient caused by indentation can drive water to diffuse out of the contact region and, hence, cause relaxation. Most of the relaxation occurred within the first few minutes of image acquisition (fig. S14). Because the scan of confocal imaging started from the bottom of the gel substrate, the short relaxation relative to the imaging time implies that the gel was in a relaxed state during image acquisition near the hydrogel surface. This allows us to treat the gel as in its relaxed state and apply the compressible neo-Hookean constitutive relation to derive stress and traction fields from the measured strain fields.

The *XZ* plane of the fluorescent image (Fig. 3A) shows that the pillar was bent toward the negative *X* direction (i.e., opposite to the direction of shear), indicating that its leading edge was subjected to a substantial lateral force. Bending of the pillar followed a trend

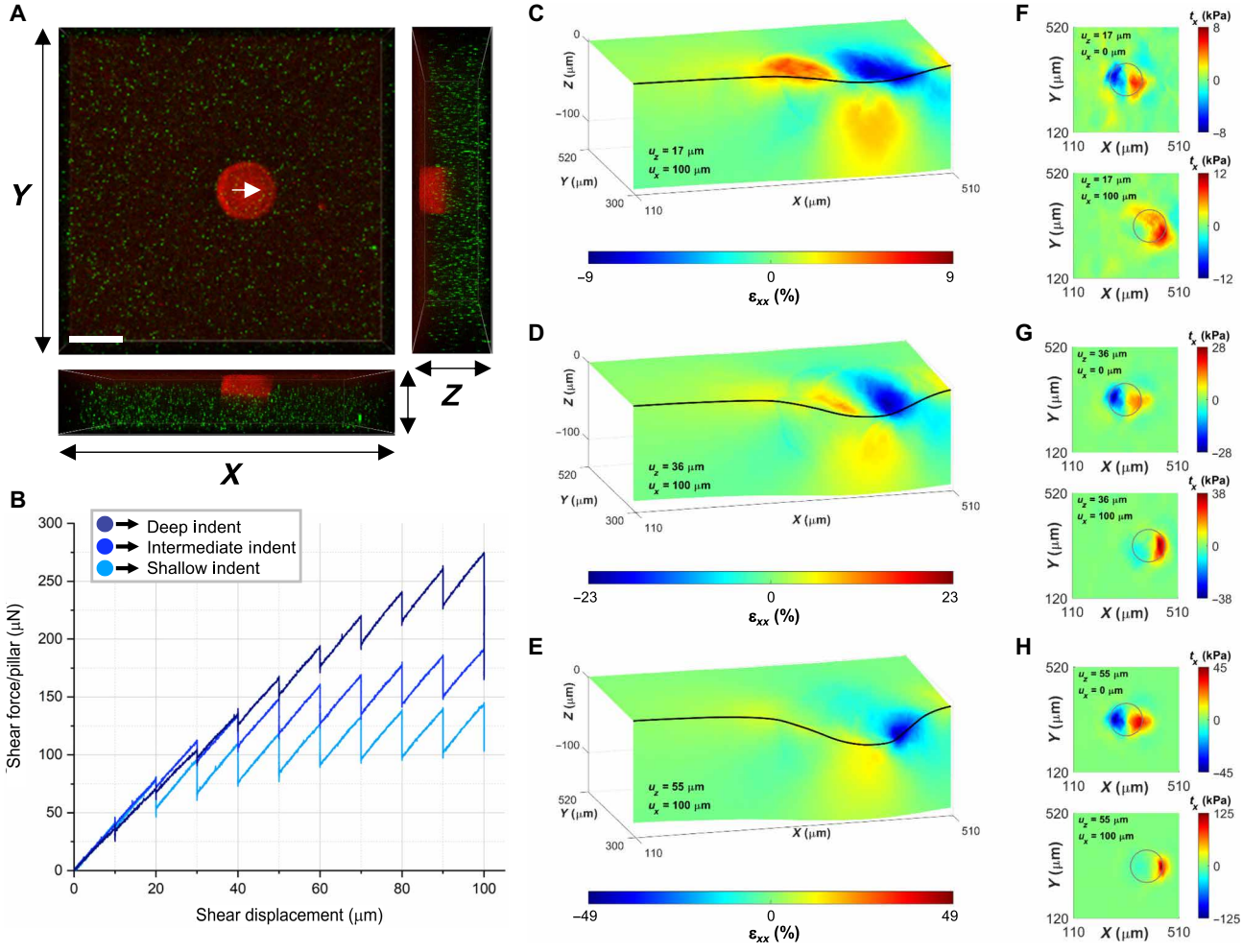

Fig. 3. Lateral contact governs shear force per pillar. (**A**) Orthogonal views of raw confocal microscopy image stacks with shear displacement in the *X* direction. The white arrow on the red fluorescent pillar denotes the direction of shear displacement. Scale bar, 100 μm. (**B**) Shear force per pillar versus shear displacement for circular pillars under different normal indentation depths. These data were obtained from the confocal microscopy experiments under stepwise displacement loading and, hence, exhibited step-like force relaxations between two loading steps. The black arrows in the legend denote the direction of shear displacement. (**C** to **E**) 3D strain field (ε_{xx}) at a shear displacement of 100 μm for (C) shallow, (D) intermediate, and (E) deep indentation. The vertical cross section represents the *XZ* plane at the central cross section of the circular pillar. (**F** to **H**) Surface traction (t_x) under shear displacement of 0 and 100 μm for (F) shallow, (G) intermediate, and (H) deep normal indentations. The contour plots in (F) to (H) are cropped from the full imaging window to focus on the area around the pillar.

similar to the shear force when the shear displacement was increased (fig. S15). The 3D strain and stress fields provide more direct evidence of lateral contact at the leading edge. Using the particle tracking method, we evaluated the 3D strain and stress fields in the hydrogel substrate for the three cases with increasing normal indentation depth. The 3D fields of Hencky strain component ε_{xx} at maximum shear displacement (100 μm) exhibit a compressive region around the leading edge of the pillar and a tensile region around the trailing edge (Fig. 3, C to E). As the normal indentation depth was increased, the compressive region became more concentrated, accompanied by a considerable increase in the maximum compressive strain (i.e., from 9 to 49%). We evaluated the distributions of traction **t** on the top surface of the deformed hydrogel substrate using the experimentally derived stress fields to reveal which surface region governs the shear force. Contour plots of t_x on the deformed hydrogel substrate surface, when projected onto the *XY* plane (Fig. 3, F to H), highlight the transition from a symmetric distribution at zero shear displacement to substantially asymmetric at maximum shear displacement (100 μm). Specifically, the distribution of t_x at maximum shear displacement features a concentrated region at the leading edge of the pillar that coincides with the region of compressive ε_{xx} (Fig. 3, C to E). Similar to the compressive strain region, the concentrated region of t_x at maximum shear displacement became more focused at the leading edge with the maximum traction $|t_x|$, increasing from 11 to 124 kPa as the normal indentation was increased. In contrast, the traction component t_y, perpendicular to the direction of shear, remained approximately symmetric at the maximum shear displacement (fig. S16). Together, the strain and traction fields provide direct evidence that the shear force per pillar is governed by the contact pressure in the lateral contact region, rather than the native friction at the bottom surface of the pillar.

Qualitatively, the shear force per pillar data in Fig. 3B exhibit a clear trend of increasing shear force with increasing indentation depth that mirrors the trend in the benchtop experiments (Fig. 1C). However, quantitatively, the maximum shear forces achieved in the confocal microscopy experiments (Fig. 3B) are four to five times of those achieved in the benchtop experiments (Fig. 1C). This discrepancy is attributed to the different schemes of displacement loading: continuous loading (benchtop experiments) versus stepwise loading (confocal microscopy experiments). Specifically, at small shear displacements, the shear force per pillar under continuous loading (e.g., ~35 μN at 10 μm for deep indent in Fig. 1C) was comparable to that under stepwise loading (e.g., ~38 μN at 10 μm for deep indent in Fig. 3B). As the shear displacement was increased, the shear force per pillar under continuous loading (Fig. 1C) changed from a linear function of shear displacement to approximately constant, indicating a transition from anchoring to sliding. In contrast, under stepwise loading (Fig. 3B), the shear force per pillar continued to increase with the shear displacement, indicating a growing lateral contact region facilitated by substrate relaxation. This effect will be further discussed in the following section with different pillar geometries.

Pillar geometry affects size and intensity of lateral contact

Motivated by results of the benchtop experiments (Fig. 1D), we performed confocal microscopy experiments for the square, clover, and buffalo pillars following the same procedures as those for the circular pillar (fig. S17). These experiments were subjected to a range of indentation depths (38 to 46 μm) comparable to the intermediate indentation for circular pillar (36 μm). The shear force data (fig. S18) are scaled by the number of pillars and are presented in Fig. 4A versus the shear displacement. We show the 3D fields of strain component ε_{xx} (Fig. 4, B to D) and the distribution of traction t_x on the hydrogel surfaces (Fig. 4, E to G) for each pillar geometry. These plots share a common feature with those for the circular pillar (Fig. 3, D and G): the transition from an approximately symmetric pattern of t_x at zero shear displacement to an asymmetric pattern of t_x biased toward the leading edge at maximum shear displacement. In contrast, the t_y distributions remain approximately unchanged before and after shear displacement (figs. S19 to S21). In addition, the concentrated region of negative t_x at maximum shear displacement coincides with the compressive region of ε_{xx} at the leading edge of the pillar, thus reaffirming the governing role of lateral contact in the shear response.

A close examination of the t_x plots at maximum shear displacement reveals the nuanced effects of pillar geometry on lateral contact. First, despite the largest indentation depth (46 μm), the square pillar exhibited the smallest magnitude of traction t_x ($\leq$17 kPa) and, consequently, one of the lowest values for shear force per pillar. This observation indicates that a flat leading edge leads to smaller lateral contact pressure than a convex leading edge (e.g., circular pillar), which is consistent with the less severe compressive strain in the lateral contact region. Second, in comparison to the circular pillar, the clover pillar exhibited a slightly smaller magnitude of t_x ($\leq$29 kPa) and a similarly sized concentrated t_x region, hence a smaller shear force per pillar. Note that the clover pillar was oriented such that a convex protrusion dominates the lateral contact region. Third, although the magnitude of t_x for the buffalo pillar ($\leq$27 kPa) is smaller to that of circular pillar, the shear force per pillar is the largest for the buffalo pillar, which is attributed to the substantially larger region of concentrated t_x and compressive strain ε_{xx}. Specifically, the traction t_x is mainly from the region near the buffalo's head and front leg (Fig. 4G), while the rear leg did not generate much traction because of an alignment issue that caused the buffalo to slightly tilt down toward its head (fig. S21).

The observations above reveal that the geometry of the pillar's leading edge governs the size and intensity of lateral contact. On one hand, the convex protrusion on the leading edge of circle and clover pillars serves to intensify the lateral contact pressure. More convex protrusions distributed along the jagged leading edge of the buffalo pillar provide more points of concentrated pressure within the lateral contact region. On the other hand, the square pillar features a straight leading edge that enlarges the lateral contact region relative to a curved profile (e.g., circle pillars). We hypothesize that the enhanced shear force from the buffalo pillar results from a trade-off between the geometric advantages of the circle and square pillars. Specifically, a longer and approximately straight geometric profile, such as the square, enlarges the lateral contact region, while the addition of convex protrusions, such as the single protrusion for the circle, increases the contact pressure and, hence, intensifies the lateral contact. To test our hypothesis, we reversed the shear direction of the buffalo pillar such that the anterior side of the buffalo became the leading edge. The anterior side features a large convex protrusion that spans the same lateral projection length as the posterior side; however, we predict that its single convex protrusion would result in a smaller lateral contact region. Therefore, a smaller shear force is expected with the anterior side as the leading edge, which was found in our experimental data (fig. S5).

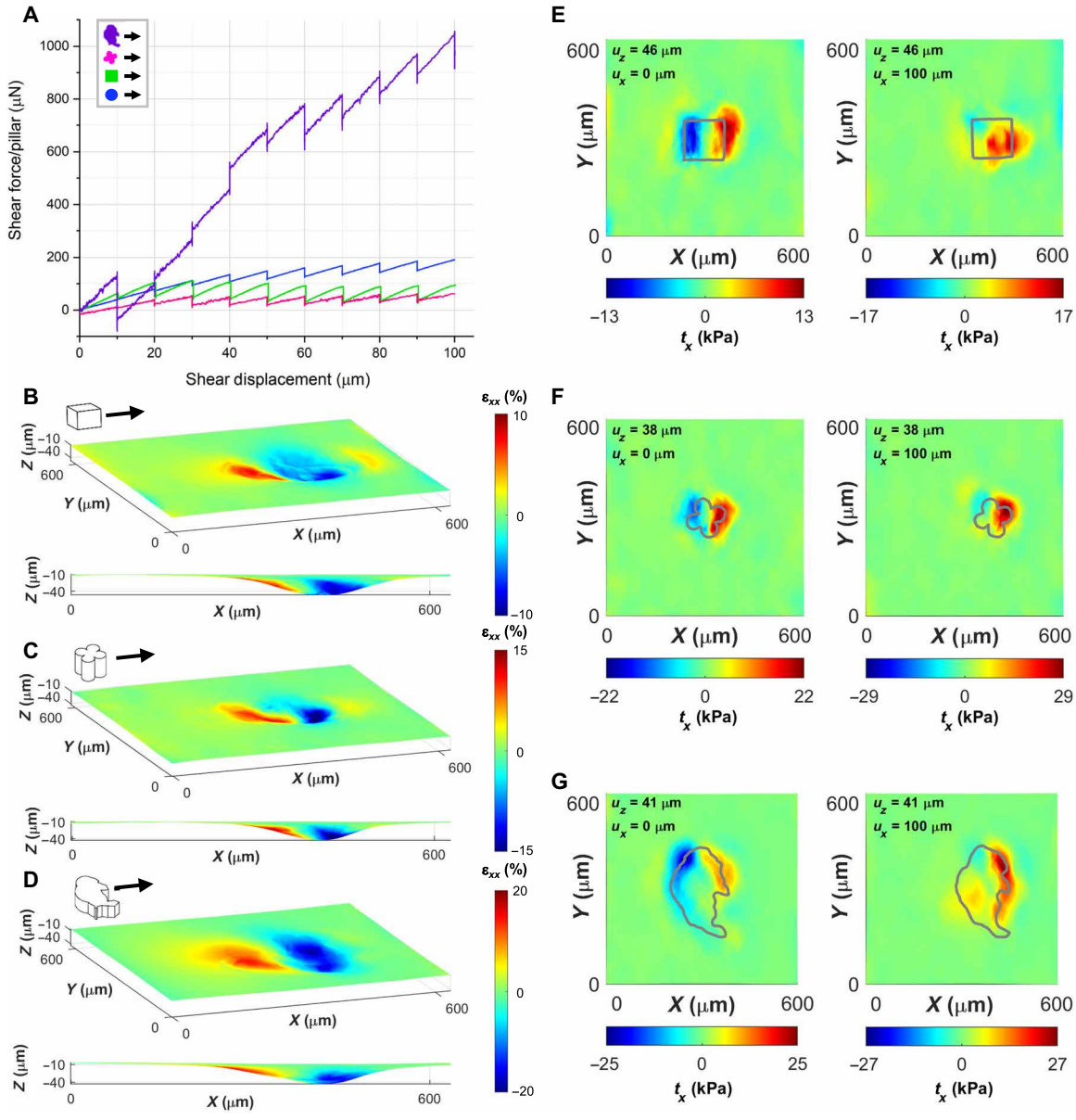

Fig. 4. Pillar geometry influences the lateral contact and shear force per pillar. (**A**) Shear force per pillar versus shear displacement for different pillar geometries. These data were obtained from the confocal microscopy experiments under stepwise displacement loading and, hence, exhibited step-like force relaxations between two loading steps. The force data for circle and square pillars were filtered by the default recursive filter on the two-axis load cell, while the force data for clover and buffalo pillars were filtered after the experiment using the same recursive filter. (**B** to **D**) Strain fields (ε_{xx}) on the hydrogel substrate surface for each pillar geometry viewed in the *XY* and *XZ* planes: (B) square, (C) clover, and (D) buffalo. (**E** to **G**) Surface tractions (t_x) on the hydrogel substrate for each pillar geometry: (E) square, (F) clover, and (G) buffalo, highlighting the influence of pillar geometry on shear traction. The gray traces indicate the position of the pillar at the contact interface extracted from the red fluorescence signal in each corresponding image stack.

Comparison between the shear force per pillar under continuous loading (Fig. 1D) or stepwise loading (Fig. 4A) further suggests that substrate relaxation can promote the growth of lateral contact. Under continuous loading (Fig. 1D), all pillar geometries showed a transition from anchoring to sliding. Under stepwise loading (Fig. 4A and fig. S18), the square and clover pillars also exhibited similar anchoring-to-sliding transitions and, hence, comparable values of shear force per pillar (~50 μN) to those under continuous loading. In contrast, the shear force for circular and buffalo pillar continued to increase under stepwise loading and became much larger than its counterpart under continuous loading. This difference explains why the circular pillar exhibited almost the same shear force per pillar as the square and clover pillars under continuous loading (Fig. 1D) but much higher shear force per pillar under stepwise loading (Fig. 4A). We attribute this difference to the geometry of the pillar's leading edge. The circular pillar features a round protrusion that allows further growth of the lateral contact region upon substrate relaxation. However, the small

protrusion size of the clover pillar and the flat leading edge of the square pillar may result in a lack of room for growing the lateral contact region.

DISCUSSION

Using a particle tracking method to experimentally map the 3D deformation fields of hydrogels upon normal and shear contact with micropillars, we obtained direct evidence that contact between the lateral surface of a pillar and the deformed hydrogel surface governs the shear force per pillar. Intensity of the lateral contact pressure increases with the indentation depth, which results in a larger shear force. Unlike dry friction on stiff surfaces, the shear force due to lateral contact is not directly dependent on the normal force (or normal contact pressure) but relies on the geometry of the pillar and deformed gel substrate. This point is supported by the experimental data for different pillar geometries. Although the four pillar geometries exhibited similar average normal contact pressure (fig. S7), they showed very different shear forces scaled by the cross-sectional area (fig. S6). In particular, the buffalo pillar shows asymmetric shear force response when the anterior or the posterior side of the buffalo is the leading edge (fig. S5). These findings highlight the important role of the pillar's geometry. Specifically, we found that geometry of the pillar's leading edge, facing the shear direction, influences both the intensity and extent of lateral contact. A jagged leading edge with a straight geometric profile (i.e., posterior side of the buffalo pillar) offers a trade-off between enhancing the lateral contact pressure and enlarging the lateral contact area. For non-axisymmetric pillars (e.g., square and buffalo), the geometry of the leading edge depends on the pillar orientation relative to the shear direction, which may offer a route toward achieving tunable or direction-dependent shear traction in future study. More broadly, the shear force collectively generated by an array of pillars will also depend on their spatial arrangement, either periodic or random, and statistical variations in the geometry of individual pillars. Understandings at the single-pillar level can lay the foundation for future works to account for the effects of spatial arrangement and statistical variations in pillar geometry.

It is worth emphasizing that the pillars adopted in this work have sharp edges where the flat end surface joins the vertical lateral surface (fig. S2). This sharp edge is critical for establishing lateral contact. If the pillar is replaced by a sphere (*40*), we observed that the shear force always relaxed to zero under stepwise loading (section S4 and fig. S22), indicating the absence of lateral contact, as opposed to the pillars with sharp edges. This observation reaffirms that the lateral contact is a geometrical effect that relies on both the indenter geometry and large deformation of the substrate. On the other hand, the sharp edge can also cause stress concentration, which may lead to damage or fracture in the hydrogel substrate under excessively deep indentation. Although substrate fracture was not observed in our experiments, it needs to be considered in the design for practical applications.

Results in this work not only provide physical insights into designing micropatterned surfaces for enhanced traction on hydrogel or tissue substrates but also demonstrate the possibility of mapping 3D deformation fields through particle tracking. The experimental method and physical insights presented here would be useful for many fields involving soft material friction, especially in bioengineering and medical devices.

MATERIALS AND METHODS

Polyacrylamide hydrogel preparation

Polyacrylamide hydrogels were prepared with 20% total polymer content (w/v) and 3% cross-linker concentration (w/w) following the protocol outlined previously (*40*, *51*). The gel precursor solution was mixed with green fluorescent microspheres (diameter = 700 nm) (Thermo Fisher Scientific, Waltham, MA) to reach a final concentration of 2.3×10^8 microspheres/ml in the hydrogel. Hydrogel substrates were bonded to an activated coverslip (*57*) and allowed to swell to equilibrium for 24 hours before each experiment.

Fluorescent micropatterned indenter fabrication

PDMS micropatterned surfaces were prepared from a master SU-8 photolithography mold and glued to the tip of the aluminum indenter. The master mold (100 μm in height) was fabricated from two 50-μm layers of an SU-8 3050 photoresist (MicroChem) on a clean silicon wafer. The first layer of SU-8 3050 was spin-coated for 30 s at 500 rpm followed by 40 s at 3000 rpm. The SU-8 edge bead was manually removed using a cotton swab dipped in an SU-8 developer. After spin-coating, the wafer was placed on a hot plate for 15 min at 75°C (temperature was slowly ramped up from room temperature and then back down). After the pre-exposure bake, the second layer of SU-8 3050 was added following the steps above, resulting in a 100-μm-thick layer. After the second pre-exposure bake, the wafer was exposed to ultraviolet light (365 nm, 9.5 mW/cm^2) for 68 s through a chrome photolithography mask (Front Range Photomask, Lake Havasu City, AZ) using a mask aligner (Karl Suss, MJB 3). The mask included several patterns with varying cross-sectional geometries including circles, squares, clovers, and buffaloes. The wafer was then transferred to a hot plate for 1 hour at 55°C (temperature was slowly ramped up from room temperature and then back down) for the postexposure bake. When the hot plate reached room temperature, the wafer was placed in a bath of an SU-8 developer (MicroChem) and agitated for 20 min to remove the uncured photoresist. After development, the wafer was rinsed with isopropyl alcohol and air-dried with nitrogen and then placed on the hot plate for 5 min at 150°C (temperature was slowly ramped up from room temperature and then back down) to ensure that the photoresist is completely cross-linked.

The SU-8 mold was treated with (3-aminopropyl)trimethoxysilane (Sigma-Aldrich) by vacuum deposition in a desiccator for 30 min before uncured PDMS (10:1 weight ratio; Dow Corning) was poured into the mold. Uncured PDMS was added to the mold until the backing layer of the micropatterned surfaces reached 1 mm in height. The PDMS was degassed for 30 min in a desiccator and then heat-cured in an oven at 60°C overnight. The PDMS micropatterned surfaces were removed from the mold and fluorescently dyed with a 100 nM rhodamine B (Sigma-Aldrich, St. Louis, MO) solution, diluted in deionized water, by soaking for 4 hours to ensure that the dye was absorbed. Then, fluorescent micropatterned surfaces were affixed to an aluminum indentation probe using a polyurethane adhesive (Gorilla Glue, Cincinnati, OH).

Benchtop experiments

Two-axis force and displacement data were collected using the custom-built MIV system (*40*) during indentation and shear experiments for several PDMS pillar surfaces with varying pillar cross-sectional geometries to evaluate the shear traction on hydrogel substrates. The cross-sectional geometries of the PDMS pillars

included circle, square, clover, and buffalo (Fig. 1A). Each PDMS pillar surface and the polyacrylamide hydrogel samples were prepared as described in the previous sections. All experiments were performed with the hydrogel sample submerged in deionized water to minimize adhesion effects and to maintain sample hydration and consistent mechanical properties during experiments.

Before each set of experiments, a PDMS-coated spherical indenter (500 μm in diameter; steel ball bearing, McMaster-Carr, Elmhurst, IL) was used to measure the mechanical properties of the hydrogel sample to ensure consistency for comparison between different PDMS pillar surfaces (section S5 and fig. S23). Following spherical indentation, the PDMS pillar probe was installed on the MIV system. The circle, square, and clover pillar probes included seven pillars arranged in a hexagonal pattern, and the buffalo pillar probe included one single pillar at the center of the indenter (Fig. 1A). Orientation of the pillars relative to the shear direction was manually controlled during the installation process and confirmed by visual inspection. For each experiment, the probe was manually lowered by the micromanipulator to hover above the submerged hydrogel sample. The surface of the hydrogel, or zero point, was identified by lowering the indenter at 0.2 μm/s until a nonzero force was measured by the load cell and then retracted back to a position of 10 μm above the hydrogel sample using the normal piezoelectric actuator. The indenter started 10 μm above the surface to ensure that the zero point could be later identified from the normal force versus normal displacement curves. For analysis, the normal indentation depth before shear displacement was determined using the zero point as a reference (fig. S24). The normal indentation was followed by the application of shear displacement under fixed normal indentation depth. A series of tests were run for each pillar probe under shallow (13 to 18 μm), intermediate (33 to 38 μm), or deep (53 to 58 μm) indentation with three replicates for each indentation depth. All indentation and shear tests were conducted with a loading velocity (0.2 μm/s) (on both axes) and a data collection rate of 5 Hz.

For each combination (normal indentation depth and pillar geometry), the average and SD of data points on the curve were calculated at 1-μm increments of shear displacement. Last, the shear force versus shear displacement curves (three replicates) were presented as one line with shaded error bars (fig. S4). Different scaling methods for the shear force are described and discussed in the Supplementary Materials (section S2 and table S1).

Confocal microscopy experiments

The MIV system was mounted on an LSCM for the microscopy experiments. Fluorescent PDMS pillar probes or PDMS-coated spherical indenters were loaded in normal and shear directions against a ~500-μm-thick polyacrylamide hydrogel substrate with embedded fluorescent particles. Hydrogels were submerged in deionized water for the duration of the experiment to prevent substrate dehydration and to minimize adhesion. The same pillar probes used in the benchtop experiments, i.e., seven-pillar probes for circle, square, and clover geometries and one-pillar probe for the buffalo geometry, were used here. The circle, square, and clover pillar geometries were much smaller than the buffalo one and, therefore, required more pillars on the probe to enable force measurement with sufficient resolution using the two-axis load cell. The probes were fabricated with ample spacing between pillars (i.e., the center-to-center distance is roughly four times the pillar width) to study single-pillar mechanics without coupled interactions from neighboring pillars on the probe (*58*). All PDMS probes were dyed by red fluorescence to enhance the contrast with the green fluorescent particles embedded in the hydrogel substrate. Similar to the benchtop experiments, we manually controlled the orientation of the pillars relative to the shear direction when installing the probes on the MIV system and confirmed the orientation through the microscope. Stepwise loading was used for all experiments with increments of 10-μm normal indentation or shear displacement for each step at a loading rate of 0.2 μm/s. Between two consecutive increments, the normal and shear displacements were held fixed for confocal image acquisition. A recursive digital filter was implemented by the digital sensor card (Mantracourt Electronics Ltd., UK) of the two-axis load cell on the MIV system. Briefly, rather than recording each input value from the load cell sensor, the filter added a fraction of the difference between the input value and the current filter output value (i.e., the difference divided by a preset filter step size) to the current filter output value and recorded it as the new filter output. If the difference between the input value and the current filter output value exceeded a preset threshold, then the filter output was set equal to the input value to allow a fast response to rapidly changing input signals. The filter step size was set to the same as the data collection frequency of the load cell sensor. When the filter was turned off, the unfiltered force data (fig. S25) were noisier but showed the same behavior as the filtered data.

The probe was lowered near the surface of the hydrogel substrate by manual adjustment of the coarse normal Z displacement manipulator on the MIV system to approach the hydrogel surface. Once the indenter was near the surface of the hydrogel, the fine normal displacement piezoelectric actuator was used to find the point of initial contact to start the experiment. From this point onward, stepwise normal indentation was initiated using the fine normal displacement piezoelectric actuator. Once the maximum normal displacement was achieved, the shear displacement was applied under a fixed normal displacement. The forces and displacements along the normal and shear directions were recorded using the two-axis load cell on the MIV system. At each step, the LSCM acquired an image stack of the fluorescent PDMS micropatterned indenter (red) and the hydrogel with embedded fluorescent tracer particles (green) on separate image channels (Fig. 3A). Image stacks were acquired with a Nikon A1R LSCM using a Plan Apochromat 20× air objective (numerical aperture = 0.75) with the pinhole set to 1 airy unit (17.9 μm for the 488-nm laser). Resolution limits under this imaging setting are estimated in section S6, which are sufficient for imaging the fluorescent particles. To reduce imaging time, we adopted a scanning setup to acquire image stacks that were 1024 pixels by 1024 pixels (0.62 μm per pixel) in the XY plane and 216 frames along the Z direction (with a 0.7-μm Z-step size), representing a scan volume of 634.88 μm by 634.88 μm by 151.2 μm. Channel series was used for image acquisition to minimize spectral bleed between channels.

Image processing

Before image analysis, a 1-pixel-width Gaussian filter was applied to both the red and green channels of each 3D image stack in the time series using IMARIS (Bitplane, Zürich, Switzerland), a commercial microscopy image analysis software. The 3D coordinates of each fluorescent tracer particle were identified using the Spots object detection tool in IMARIS (fig. S26 and movie S1). This tool models

point-like structures in the 3D image stacks given parameters for automatic detection. For each set of 3D image stacks, the *XY* spot diameter was estimated as 10 μm and the *Z* spot height was estimated as 3 μm for each spot. Once the Spots tool identified particles on the green channel in each 3D image stack within the time series, the automatic threshold for the quality filter was determined to filter beads smaller or larger than the estimated size given above. An additional filter was added to filter out any identified spots on the green channel that had red fluorescence in the same location over a certain threshold. This filter was added to eliminate any beads floating in the deionized water above the gel that were stuck to the PDMS pillars and, therefore, not embedded in the polymer matrix. Because of the refractive index mismatch between the objective immersion medium and the sample immersion medium in the experiments, we implemented an axial scaling factor to correct the *Z* coordinate of each fluorescent particle (section S7 and fig. S27).

Particle tracking method

Following fluorescent particle identification, particle coordinates were tracked through the time series using the Autoregressive Motion algorithm within the IMARIS Spots tool (fig. S26). This algorithm uses an autoregressive AR1 process to model the particle trajectories by looking back one time point and predicting that the identified particle will move the same distance in the same direction. The Maximum Distance parameter was set to 10 μm, which allows the particle to deviate this distance from the predicted position. In addition, the Maximum Gap Size parameter was set to three, which allows a particle to disappear for three consecutive time points and continue the track lineage. This prevents track fragments by using a gap-closing algorithm to connect objects associated with the same spot track. When all particles have been successfully tracked through the time series, the particle coordinates and track lineage information were exported to an Excel (Microsoft, Redmond, WA) file using the Statistics tool and further analyzed with a custom MATLAB (MathWorks, Natick, MA) script. Alternatively, particle tracking can be achieved by leveraging the randomness of the spatial distribution of particles, i.e., to use the relative positions of neighboring particles as the signature to track an individual particle (*46*). This method yields similar results to the IMARS-based tracking, as demonstrated by the benchmark problem of spherical indentation (section S8 and fig. S28), but takes much longer computational time than IMARIS tracking.

We implemented the MLS interpolation scheme to construct continuous displacement fields from discrete particle displacements (*44*). The mathematical formulation of the interpolation scheme and the evaluation of 3D Hencky strain tensor $\boldsymbol{\varepsilon}$ (*45*), also known as the true strain tensor, are summarized in section S9. To calculate the 3D stress field, we modeled the hydrogel as a compressible neo-Hookean solid with the two parameters, shear modulus μ and Poisson's ratio ν, calibrated experimentally (*59*, *60*), yielding μ = 37.5 kPa and ν = 0.362 (section S3). Using this model, we calculated the Cauchy stress tensor $\boldsymbol{\sigma}$, also known as the true stress tensor (section S9). The compressible hyperelastic model adopted for the hydrogel substrate, despite the typically observed time-dependent mechanical behaviors (e.g., viscoelasticity and poroelasticity), is justified by the slow loading rate during a loading increment and the long imaging time between two loading increments, which renders the hydrogel in its long-term relaxed limit (fig. S9).

To evaluate the surface traction, we used the built-in MATLAB function "surfnorm" to perform a bicubic fit to identify the normal vector $\mathbf{n}$ of the deformed contact surface. Briefly, we first discretized the undeformed, flat hydrogel surface by a square grid. At each node of this grid, the traction $\mathbf{t}$ is given by $\mathbf{t} = \boldsymbol{\sigma}\mathbf{n}$, where $\boldsymbol{\sigma}$ is the Cauchy stress tensor. The total reaction force, F_k in Eq. 1, is equal to the area integral of the traction t_k

$$F_k = \int t_k \, dS = \int (\sigma_{kx} n_x + \sigma_{ky} n_y + \sigma_{kz} n_z) \, dS, (k = x, y, \text{or } z) \quad (1)$$

This area integral was calculated by summing the equivalent reaction force at each node, defined as the traction at a node multiplied by the partial surface area assigned to the node (fig. S29). The partial surface area assigned to a node is taken as the sum of a quarter of each parallelogram that shares the same node.

Finite element model

A finite element model was built for the benchmark problem of spherical indentation. The model consisted of a rigid sphere coated by a thin layer of PDMS and a hydrogel substrate matching the experimental geometry. We leveraged the symmetry of the problem, built a model capturing half of the experimental geometry, and imposed symmetry boundary condition on the symmetry plane (fig. S11). The hydrogel substrate was meshed into 362076 C3D8H elements with the smallest element size equal to 8 μm, and the bottom surface was fixed. The hydrogel substrate was modeled as a compressible neo-Hookean hyperelastic solid with shear modulus μ = 37.5 kPa and Poisson's ratio ν = 0.362, which are the same as those used for calculating the stress fields using the strain fields measured from particle tracking. The PDMS coating was modeled as a neo-Hookean solid with a shear modulus of 1 MPa (*41*), which is practically rigid relative to the hydrogel substrate. The contact between the PDMS-coated indenter and the hydrogel substrate was assumed to be frictionless.

SUPPLEMENTARY MATERIALS

Supplementary material for this article is available at https://science.org/doi/10.1126/sciadv.abn2728

REFERENCES AND NOTES

1. C. W. McCutchen, The frictional properties of animal joints. *Wear* **5**, 1–17 (1962).
2. Z. M. Jin, D. Dowson, J. Fisher, The effect of porosity of articular cartilage on the lubrication of a normal human hip joint. *Proc. Inst. Mech. Eng. Part H J. Eng. Med.* **206**, 117–124 (1992).
3. Z. M. Jin, J. Zheng, W. Li, Z. R. Zhou, Tribology of medical devices. *Biosurface Biotribology* **2**, 173–192 (2016).
4. L. K. Bowen, K. Johannes, E. Zuetell, K. N. Calahan, S. A. Edmundowicz, R. Long, M. E. Rentschler, Patterned enteroscopy balloon design factors influence tissue anchoring. *J. Mech. Behav. Biomed. Mater.* **111**, 103966 (2020).
5. G. A. Formosa, J. M. Prendergast, S. A. Edmundowicz, M. E. Rentschler, Novel optimization-based design and surgical evaluation of a treaded robotic capsule colonoscope. *IEEE Trans. Robot.* **36**, 545–552 (2019).
6. R. Hensel, K. Moh, E. Arzt, Engineering micropatterned dry adhesives: From contact theory to handling applications. *Adv. Funct. Mater.* **28**, 1800865 (2018).
7. B. Persson, Wet adhesion with application to tree frog adhesive toe pads and tires. *J. Phys. Condens. Matter* **19**, 376110 (2007).
8. J.-H. Dirks, W. Federle, Fluid-based adhesion in insects—Principles and challenges. *Soft Matter* **7**, 11047–11053 (2011).
9. L. J. Sliker, X. Wang, J. A. Schoen, M. E. Rentschler, Micropatterned treads for in vivo robotic mobility. *J. Med. Device* **4**, 041006 (2010).
10. L. J. Sliker, M. D. Kern, J. A. Schoen, M. E. Rentschler, Surgical evaluation of a novel tethered robotic capsule endoscope using micro-patterned treads. *Surg. Endosc.* **26**, 2862–2869 (2012).

11. M. Varenberg, S. N. Gorb, Hexagonal surface micropattern for dry and wet friction. *Adv. Mater.* **21**, 483–486 (2009).
12. L. Xue, J. Iturri, M. Kappl, H.-J. Butt, A. del Campo, Bioinspired orientation-dependent friction. *Langmuir* **30**, 11175–11182 (2014).
13. L. Xue, B. Sanz, A. Luo, K. T. Turner, X. Wang, D. Tan, R. Zhang, H. Du, M. Steinhart, C. Mijangos, M. Guttmann, M. Kappl, A. Del Campo, Hybrid surface patterns mimicking the design of the adhesive toe pad of tree frog. *ACS Nano* **11**, 9711–9719 (2017).
14. E. Andablo-Reyes, M. Bryant, A. Neville, P. Hyde, R. Sarkar, M. Francis, A. Sarkar, 3D biomimetic tongue-emulating surfaces for tribological applications. *ACS Appl. Mater. Interfaces* **12**, 49371–49385 (2020).
15. H. Chen, L. Zhang, D. Zhang, P. Zhang, Z. Han, Bioinspired surface for surgical graspers based on the strong wet friction of tree frog toe pads. *ACS Appl. Mater. Interfaces* **7**, 13987–13995 (2015).
16. J. Kwon, E. Cheung, S. Park, M. Sitti, Friction enhancement via micro-patterned wet elastomer adhesives on small intestinal surfaces. *Biomed. Mater.* **1**, 216–220 (2006).
17. P. van Assenbergh, M. Fokker, J. Langowski, J. van Esch, M. Kamperman, D. Dodou, Pull-off and friction forces of micropatterned elastomers on soft substrates: The effects of pattern length scale and stiffness. *Beilstein J. Nanotechnol.* **10**, 79–94 (2019).
18. A. Sarkar, E. Andablo-Reyes, M. Bryant, D. Dowson, A. Neville, Lubrication of soft oral surfaces. *Curr. Opin. Colloid Interface Sci.* **39**, 61–75 (2019).
19. E. Liamas, S. D. Connell, S. N. Ramakrishna, A. Sarkar, Probing the frictional properties of soft materials at the nanoscale. *Nanoscale* **12**, 2292–2308 (2020).
20. E. Liamas, S. D. Connell, M. Zembyla, R. Ettelaie, A. Sarkar, Friction between soft contacts at nanoscale on uncoated and protein-coated surfaces. *Nanoscale* **13**, 2350–2367 (2021).
21. J. Delavoipiere, Y. Tran, E. Verneuil, B. Heurtefeu, C. Yuen Hui, A. Chateauminois, Friction of poroelastic contacts with thin hydrogel films. *Langmuir* **34**, 9617–9626 (2018).
22. J. Gong, M. Higa, Y. Iwasaki, Y. Katsuyama, Y. Osada, Friction of gels. *J. Phys. Chem. B* **101**, 5487–5489 (1997).
23. E. R. Reale, A. C. Dunn, Poroelasticity-driven lubrication in hydrogel interfaces. *Soft Matter* **13**, 428–435 (2017).
24. B. N. J. Persson, Some comments on hydrogel and cartilage contact mechanics and friction. *Tribol. Lett.* **66**, 23 (2018).
25. S. Yashima, N. Takase, T. Kurokawa, J. P. Gong, Friction of hydrogels with controlled surface roughness on solid flat substrates. *Soft Matter* **10**, 3192–3199 (2014).
26. T. Yamamoto, T. Kurokawa, J. Ahmed, G. Kamita, S. Yashima, Y. Furukawa, Y. Ota, H. Furukawa, J. P. Gong, In situ observation of a hydrogel-glass interface during sliding friction. *Soft Matter* **10**, 5589–5596 (2014).
27. T. Shoaib, J. Heintz, J. A. Lopez-Berganza, R. Muro-Barrios, S. A. Egner, R. M. Espinosa-Marzal, Stick-slip friction reveals hydrogel lubrication mechanisms. *Langmuir* **34**, 756–765 (2018).
28. G. Kagata, J. P. Gong, Y. Osada, Friction of gels. 6. Effects of sliding velocity and viscoelastic responses of the network. *J. Phys. Chem. B* **106**, 4596–4601 (2002).
29. A. C. Dunn, J. M. Urueña, Y. Huo, S. S. Perry, T. E. Angelini, W. G. Sawyer, Lubricity of surface hydrogel layers. *Tribol. Lett.* **49**, 371–378 (2013).
30. S. Ghosh, B. Seelbinder, J. T. Henderson, R. D. Watts, A. K. Scott, A. I. Veress, C. P. Neu, Deformation microscopy for dynamic intracellular and intranuclear mapping of mechanics with high spatiotemporal resolution. *Cell Rep.* **27**, 1607–1620.e4 (2019).
31. S. Sik Hur, Y. Zhao, E. Botvinick, S. Chien, Live cells exert 3-dimensional traction forces on their substrata. *Cell. Mol. Bioeng.* **2**, 425–436 (2009).
32. C. Franck, S. Hong, S. A. Maskarinec, D. A. Tirrell, G. Ravichandran, Three-dimensional full-field measurements of large deformations in soft materials using confocal microscopy and digital volume correlation. *Exp. Mech.* **47**, 427–438 (2007).
33. S. A. Maskarinec, C. Franck, D. A. Tirrell, G. Ravichandran, Quantifying cellular traction forces in three dimensions. *Proc. Natl. Acad. Sci. U.S.A.* **106**, 22108–22113 (2009).
34. C. Franck, S. A. Maskarinec, D. A. Tirrell, G. Ravichandran, Three-dimensional traction force microscopy: A new tool for quantifying cell-matrix interactions. *PLOS ONE* **6**, e17833 (2011).
35. E. Bar-Kochba, J. Toyjanova, K.-S. Kim, C. Franck, A fast iterative digital volume correlation algorithm for large deformations. *Exp. Mech.* **55**, 261–274 (2015).
36. W. R. Legant, J. S. Miller, B. L. Blakely, D. M. Cohen, G. M. Genin, C. S. Chen, Measurement of mechanical tractions exerted by cells in three-dimensional matrices. *Nat. Methods* **7**, 969–971 (2010).
37. W. R. Legant, C. K. Choi, J. S. Miller, L. Shao, L. Gao, E. Betzig, C. S. Chen, A. R. Horwitz, Multidimensional traction force microscopy reveals out-of-plane rotational moments about focal adhesions. *Proc. Natl. Acad. Sci. U.S.A.* **110**, 881–886 (2013).
38. Y. Xu, W. C. Engl, E. R. Jerison, K. J. Wallenstein, C. Hyland, L. A. Wilen, E. R. Dufresne, Imaging in-plane and normal stresses near an interface crack using traction force microscopy. *Proc. Natl. Acad. Sci. U.S.A.* **107**, 14964–14967 (2010).
39. R. W. Style, R. Boltyanskiy, G. K. German, C. Hyland, C. W. Macminn, A. F. Mertz, L. A. Wilen, Y. Xu, E. R. Dufresne, Traction force microscopy in physics and biology. *Soft Matter* **10**, 4047–4055 (2014).
40. K. G. Johannes, K. N. Calahan, Y. Qi, R. Long, M. E. Rentschler, Three-dimensional microscale imaging and measurement of soft material contact interfaces under quasi-static normal indentation and shear. *Langmuir* **35**, 10725–10733 (2019).
41. I. D. Johnston, D. K. McCluskey, C. K. L. Tan, M. C. Tracey, Mechanical characterization of bulk Sylgard 184 for microfluidics and microengineering. *J. Micromech. Microeng.* **24**, 035017 (2014).
42. F. P. Bowden, D. Tabor, Mechanism of metallic friction. *Nature* **150**, 197–199 (1942).
43. F. P. Bowden, D. Tabor, *The Friction and Lubrication of Solids* (Clarendon Press, 1954).
44. T. Belytschko, Y. Y. Lu, L. Gu, Element-free Galerkin methods. *Int. J. Numer. Methods Eng.* **37**, 229–256 (1994).
45. W. Liu, R. Long, Constructing continuous strain and stress fields from spatially discrete displacement data in soft materials. *J. Appl. Mech.* **83**, 011006 (2015).
46. Y. Qi, Z. Zou, J. Xiao, R. Long, Mapping the nonlinear crack tip deformation field in soft elastomer with a particle tracking method. *J. Mech. Phys. Solids* **125**, 326–346 (2019).
47. M. S. Hall, R. Long, C. Y. Hui, M. Wu, Mapping three-dimensional stress and strain fields within a soft hydrogel using a fluorescence microscope. *Biophys. J.* **102**, 2241–2250 (2012).
48. M. Galluzzi, C. S. Biswas, Y. Wu, Q. Wang, B. Du, F. J. Stadler, Space-resolved quantitative mechanical measurements of soft and supersoft materials by atomic force microscopy. *NPG Asia Mater.* **8**, e327 (2016).
49. Q. Wang, C. S. Biswas, M. Galluzzi, Y. Wu, B. Du, F. J. Stadler, Random copolymer gels of N-isopropylacrylamide and N-ethylacrylamide: Effect of synthesis solvent compositions on their properties. *RSC Adv.* **7**, 9381–9392 (2017).
50. C. Sekhar Biswas, Q. Wang, M. Galluzzi, Y. Wu, S. T. Navale, B. Du, F. J. Stadler, C. S. Biswas, Q. Wang, M. Galluzzi, Y. Wu, S. T. Navale, B. Du, F. J. Stadler, Versatile mechanical and thermoresponsive properties of macroporous copolymer gels. *Macromol. Chem. Phys.* **218**, 1600554 (2017).
51. A. K. Denisin, B. L. Pruitt, Tuning the range of polyacrylamide gel stiffness for mechanobiology applications. *ACS Appl. Mater. Interfaces* **8**, 21893–21902 (2016).
52. C. H. Lee, A. J. Crosby, T. Emrick, R. C. Hayward, Characterization of heterogeneous polyacrylamide hydrogels by tracking of single quantum dots. *Macromolecules* **47**, 741–749 (2014).
53. K. Pafiti, Z. Cui, D. Adlam, J. Hoyland, A. J. Freemont, B. R. Saunders, Hydrogel composites containing sacrificial collapsed hollow particles as dual action pH-responsive biomaterials. *Biomacromolecules* **17**, 2448–2458 (2016).
54. J. Zhang, C. R. Daubert, E. A. Foegeding, Characterization of polyacrylamide gels as an elastic model for food gels. *Rheol. Acta.* **44**, 622–630 (2005).
55. M. Galli, K. S. C. Comley, T. A. V. Shean, M. L. Oyen, Viscoelastic and poroelastic mechanical characterization of hydrated gels. *J. Mater. Res.* **24**, 973–979 (2009).
56. Z. I. Kalcioglu, R. Mahmoodian, Y. Hu, Z. Suo, K. J. Van Vliet, From macro- to microscale poroelastic characterization of polymeric hydrogels via indentation. *Soft Matter* **8**, 3393–3398 (2012).
57. R. S. Fischer, K. A. Myers, M. L. Gardel, C. M. Waterman, Stiffness-controlled three-dimensional extracellular matrices for high-resolution imaging of cell behavior. *Nat. Protoc.* **7**, 2056–2066 (2012).
58. C. Poulard, F. Ed, E. Restagno, R. El Weil, L. L. Eger, Mechanical tuning of adhesion through micro-patterning of elastic surfaces †. *Soft Matter* **7**, 2543–2551 (2011).
59. Y. Hu, X. Zhao, J. J. Vlassak, Z. Suo, Using indentation to characterize the poroelasticity of gels. *Appl. Phys. Lett.* **96**, 121904 (2010).
60. E. K. Dimitriadis, F. Horkay, J. Maresca, B. Kachar, R. S. Chadwick, Determination of elastic moduli of thin layers of soft material using the atomic force microscope. *Biophys. J.* **82**, 2798–2810 (2002).

Acknowledgments: We thank the BioFrontiers Institute Advanced Light Microscopy Core Facility for equipment access and use of the Nikon A1R LSCM, supported by NIST-CU Cooperative Agreement award number 70NANB15H226. **Funding:** This work was supported by National Science Foundation grant CMMI-1636203 (to M.E.R. and R.L.). **Author contributions:** Conceptualization: K.N.C., Y.Q., K.G.J., M.E.R., and R.L. Methodology: K.N.C., Y.Q., K.G.J., M.E.R., and R.L. Investigation: K.N.C. and Y.Q. Visualization: K.N.C. and Y.Q. Supervision: M.E.R. and R.L. Writing—Original draft: K.N.C. Writing—Review and editing: K.N.C., Y.Q., K.G.J., M.E.R., and R.L. **Competing interests:** M.E.R. is a cofounder of Aspero Medical Inc., a University of Colorado spinout company that is focused on commercializing balloon overtube products for use in enteroscopy. All other authors declare that they have no competing interests. **Data and materials availability:** All data needed to evaluate the conclusions in the paper are present in the paper and/or the Supplementary Materials.

Submitted 17 November 2021
Accepted 9 May 2022
Published 24 June 2022
10.1126/sciadv.abn2728